Korean Journal of Chemical Engineering (2024) 41:2691–2703
https://doi.org/10.1007/s11814-024-00194-2

ORIGINAL ARTICLE

# Integrated Melamine Molecules on Microspherical Boehmite Particles via Spray Drying for Highly Efficient $CO_2/N_2$ Adsorption Separation

**Van Nhieu Le[1] · Duy Quang Dao[2,3] · Hai Bang Truong[4,5] · Huu Trung Nguyen[1] · Toan Minh Pham[6] · Jongwook Park[6] · Jinsoo Kim[6]**

Received: 18 March 2024 / Revised: 9 May 2024 / Accepted: 16 May 2024 / Published online: 23 May 2024


## Abstract

A newly developed spherical boehmite and melamine composite with a mesoporous structure was successfully fabricated through a spray drying system utilizing a mixture of boehmite sol and melamine. EDX–SEM, FTIR, and TGA analyses confirmed the integration of melamine into the boehmite network within the resulting composite. With an increase in melamine content, the composites exhibited a gradual reduction in porosity compared to their pristine boehmite counterpart. However, the $CO_2$ uptake of the composites continued to demonstrate improvement. The boehmite sample modified with 5 mol% of melamine (IMB#5) demonstrated the highest $CO_2$ adsorption capacity at 19.2 $cm^3\ g^{-1}$. This value surpassed the original boehmite sample by 46.1% under conditions of 25 °C and 1 bar. The enhanced adsorption can be attributed to the development of adsorptive affinity facilitated by N-derived functional groups (–$NH_2$ and –CN) within the melamine structure and their interaction with $CO_2$. As a result, the $CO_2/N_2$ separation factor and $CO_2/N_2$ adsorptive selectivity using the ideal adsorbed solution theory (IAST) over the IMB#5 sample were 113.3 and 3182, respectively, approximately 3 times and 9.2 times higher than those for the boehmite sample. Density functional theory (DFT) calculations were conducted to investigate the interaction of melamine on the boehmite surface, as well as the selective adsorption of $CO_2$ and $N_2$ gaseous molecules on the boehmite/melamine composite. It is shown that the melamine mainly interacts with the boehmite via a strong binding of the N atom of the triazine ring with the Al atom of the boehmite. The adsorption of $CO_2$ has lower binding enthalpies and free energies than that of $N_2$. These findings indicate that utilizing continuous spray drying holds promise as an effective pathway for scaling up the production of mesoporous boehmite/melamine composite spheres as $CO_2$ selective adsorbents.

**Keywords** Boehmite/melamine spherical composite · Continuous spray dryer · $CO_2/N_2$ IAST selectivity · Enhanced $CO_2$ adsorption performance · Density functional theory (DFT)

✉ Van Nhieu Le
levannhieu@iuh.edu.vn

✉ Jinsoo Kim
jkim21@khu.ac.kr

Hai Bang Truong
truonghaibang@vlu.edu.vn

[1] Faculty of Chemical Engineering, Industrial University of Ho Chi Minh City, 12 Nguyen Van Bao, Go Vap, Ho Chi Minh City 70000, Vietnam

[2] Institute of Research and Development, Duy Tan University, Da Nang 550000, Vietnam

[3] School of Engineering and Technology, Duy Tan University, Da Nang 550000, Vietnam

[4] Optical Materials Research Group, Science and Technology Advanced Institute, Van Lang University, Ho Chi Minh City 700000, Vietnam

[5] Faculty of Applied Technology, School of Technology, Van Lang University, Ho Chi Minh City 700000, Vietnam

[6] Department of Chemical Engineering (Integrated Engineering), Kyung Hee University, 1732 Deogyeong-daero, Giheung-gu, Yongin-si 17104, Gyeonggi-do, South Korea

## Introduction

The expanding population and escalating energy demand pose threats to human health and ecosystems, primarily driven by the increasing emissions of $CO_2$ into the atmosphere, contributing to climate change and global warming. Currently, anthropogenic activities, particularly the combustion process and industrial production, stand as the main sources of $CO_2$ emissions [30, 41, 49]. Thus, minimizing $CO_2$ emissions is a critical strategy for promoting sustainable development. Removal of $CO_2$ from the exhausted gas stream using means of separation such as cryogenic condensation/distillation, absorption, adsorption, and membrane has been investigated. Among them, the adsorption strategy stands out as an effective method, thanks to its simplicity, affordability, and high efficiency, particularly for low-concentration gas mixtures [11, 30, 36]. In the realm of adsorption, the adsorbent takes on a vital role within the system, wherein its unique characteristics wield significant influence over the effectiveness of gas separation. It is reported that developing adsorbents with high porosity and/or many adsorption sites having a vigorous affinity toward objective gasses is necessary to improve $CO_2$ selective adsorption [10, 19, 29]. In addition, low-cost adsorbents, abundant in raw materials and easy to produce on a large scale, are required to minimize operating costs and have high potential in industrial-scale applications. Until now, various types of adsorbents, including metal–organic frameworks (MOFs), porous polymers, activated carbons, zeolites, and metal oxides, have been investigated for this purpose. Unfortunately, no adsorbents satisfy all of the criteria mentioned above, showing that the improvement of one property usually trades off the others.

Boehmite is the most crucial precursor for producing different types of aluminium oxide through heat treatment. Boehmite is extensively used as an adsorbent, supported catalyst, filler in the membrane, and reinforced material in composite synthesis, much like transition aluminas, because it is safe, simple, and easily accessible, having a high specific surface area, surface acidic–basic properties, and thermal and mechanical stability [5, 14, 33]. Depending on the specific fabricating process employed, the resulting boehmite possesses various shapes, surface morphologies, and physicochemical properties. Traditionally, the boehmite has been produced by several routes: (i) mineral gibbsite experienced solid-state thermal decomposition; (ii) precipitation in an aqueous solution from neutralized and aged aluminum salt solutions under hydrothermal conditions; and (iii) a sol–gel procedure derived from aluminum alkoxides that involved hydrolysis and condensation steps under soft conditions, followed by a peptization stage [1, 8, 14, 22]. Compared to the others, the sol–gel-derived route requires a higher cost in preparing material; however, the obtained material has higher purity, greater uniformity, and a highly organized structure while operating at a low temperature and with high productivity [8, 9, 45]. In addition, spray drying technology often involves transforming the matter in the liquid phase into dried powder after undergoing rapid evaporation under a hot gas. The microparticle size distribution is somewhat narrow. This technology is widely used in many industries, from simple to large-scale production, that may operate on continuous production [4, 38, 44].

In the boehmite structure, double layers of oxygen octahedrons surround a central Al atom. Moreover, the unsaturated oxygen within the network bonds with hydrogen atoms to create numerous hydroxyl groups covering the surface [6, 20, 22, 28]. However, boehmite demonstrates a limited capacity for $CO_2$ adsorption because its porous structure is primarily composed of mesopores instead of micropores, leading to reduced interactive adsorption between boehmite and $CO_2$ [11, 12]. To enhance the capture of $CO_2$, it is essential to graft functional moieties with a strong affinity for the adsorbate onto the surface of boehmite. This grafting process guides the pore structure toward the micropore region, leading to a reduction in pore size. Concurrently, it augments the density of active sites on the material surface, encompassing both hydroxyl (–OH) groups and additional sites, particularly those with base-featured groups activated by $CO_2$ as a Lewis acid. This augmentation results in a notable improvement in effective adsorption, facilitated by H-bonding and/or acid–base interaction. This pathway can be easily conducted thanks to the abundant hydroxyl groups providing anchoring sites that can be easily incorporated into the functional guests via H-bonding [16, 22, 39].

This study successfully prepared modified boehmite adsorbents with a high concentration of N-derived functional groups from melamine molecules using a combination of the sol–gel and spray drying methods. With this, the new adsorption sites originating from N-derived groups of $-NH_2$ and $-CN$ contribute to improving $CO_2$ adsorption capacity despite decreased porosity in the resulting material. Several techniques, including powder X-ray diffraction (PXRD), energy dispersive X-ray/scanning electron microscopy (EDX–SEM), Fourier transform infrared spectroscopy (FTIR), thermogravimetric analysis (TGA), and nitrogen porosimetry, are used to characterize the effect of melamine concentrations on the shape, morphology, and physical–chemical properties of the resulting material. Then the adsorption–desorption isotherms of $CO_2$ and $N_2$

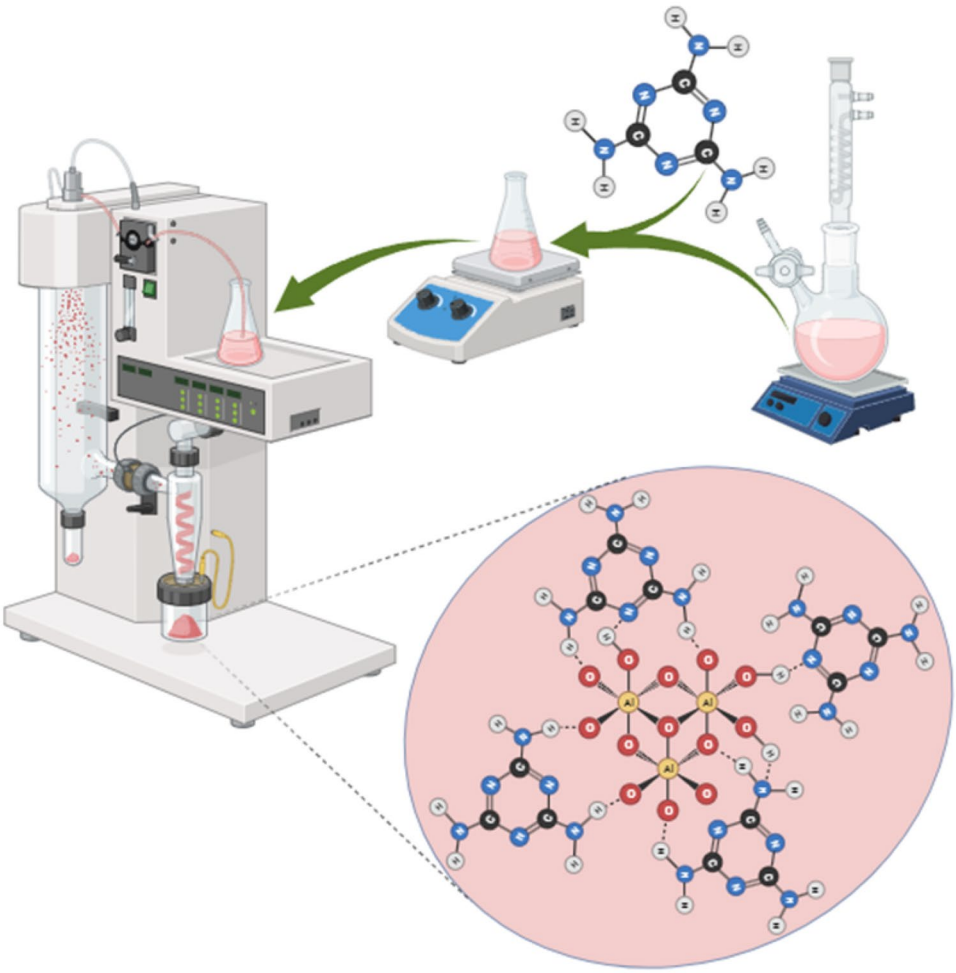

**Scheme 1** Microporous Boeh/Me sphere preparation by combining sol–gel and spray drying methods

were analyzed at various temperatures to evaluate the $CO_2$ separation performance of the materials.

## Experiment

### Materials

Aluminum isopropoxide (hereafter ALISP, 98%) and melamine ($C_3H_6N_6$, 99%) were purchased from Sigma-Aldrich. Nitric acid ($HNO_3$, 60%) was obtained from Daejung Chemical, Korea. The purified water (18.2 MΩ·cm) was produced by an Aqua Max Ultra 360 (Young-Lin, Korea). All the chemicals were used without further purification.

### Synthesis of Boehmite/Melamine Spherical Composites

The spherical boehmite/melamine composite was fabricated using a combination of the sol–gel and spray drying methods (Scheme 1). First, a highly stable boehmite sol of 0.2 M was prepared according to Yoldas's procedure with some modifications [8, 13]. Briefly, a desired amount of ALISP was hydrolyzed in 750 mL of purified water at 90 °C under stirring for 6 h. Then the nitric acid (1 M) as a peptizing agent was added to the slurry mentioned above until the ratio of $H^+/Al^{3+}$ achieved 0.07 in mole to convert the AlOOH precipitates into the colloidal sol. This process was conducted at 90 °C overnight under a reflux system. The resulting sol was obtained after exposing the colloid to the air at 90 °C for 2 h to release the alcohol remnant. Second, a calculated amount of melamine powder was dissolved in 200 mL of the boehmite sol under stirring until obtaining uniform sol. The sol was continuously stirred for 12 h at room temperature to establish the H-bonding between melamine molecules and boehmite species via the $–NH_2$, –CN, and –OH groups. Finally, the obtained sol was introduced into the spray drying system (EYELA, SD-1000) to produce the spherical composites. The sol was sprayed into the glass chamber via a 0.5-mm-diameter nozzle by a pump system with a flow rate of 0.4 $m^3\ h^{-1}$. The sol droplets were dried in the chamber by the hot air

at 175 °C and 0.25 $m^3$ $min^{-1}$. The spherical composites were collected at the bottom of the cyclone system and denoted as IMB#x, where x represents the mole percentage of melamine in the sol mixture (x = 2.5, 5.0, 7.5, and 10.0).

### Characterizations

Powder X-ray diffraction (PXRD) patterns were collected at room temperature at a scanning speed of 6° $min^{-1}$ from 10° to 70° (2θ) using XRD (MAC-18XHF, Rigaku, Japan) equipped with a Cu-Kα radiation source. The FTIR profiles of the products were recorded on Tensor 27 (Bruker, Germany) by the attenuated total reflectance method in a range of 650–4000 $cm^{-1}$. The morphology and element distribution of the composites were analyzed by field emission SEM (Leo-Supra 55, Carl Zeiss STM, Germany). The thermal stability of the obtained materials was assessed using TGA analysis (Q50, TA instrument, USA). The analysis occurred within a temperature range of 30–700 °C, employing a ramp rate of 5 K $min^{-1}$ under an $N_2$ stream. The nitrogen adsorption–desorption isotherms for the as-prepared materials were examined at 77 K with BELSORP-max (BEL, Japan). Prior to analysis, the adsorbents underwent degassing at 120 °C for 6 h under vacuum. The specific surface areas and pore size distributions were identified using the standard Brunauer–Emmett–Teller (BET) and Horvath–Kawazoe (HK) models. Most of the apparatus and equipments were supported by the Core Facility Center for Analysis of Optoelectronic Materials and Devices of the Korea Basic Science Institute (KBSI).

### $CO_2$ and $N_2$ Adsorption Experiments

$CO_2$ and $N_2$ adsorption isotherms were collected in the pressure range of 0 to 100 kPa using an adsorption apparatus (BELSORP-mini II, Bel, Japan) equipped with a system of jacketed heat exchanger, which was connected to a heating bath circulator to control the adsorption temperature. Typically, ca. 200 mg of the adsorbent was degassed first under vacuum at 393 K for 6 h. After that, the adsorbent was naturally cooled to room temperature before measuring $CO_2$ and $N_2$ gas adsorption. The adsorbent's reusability was evaluated over five cycles of $CO_2$ adsorption experiments at 298 K. Following each cycle, the adsorbent was reactivated at 393 K under vacuum conditions for a duration of 2 h.

### The Ideal Adsorbed Solution Theory (IAST) Selectivity

The ideal adsorbed solution theory (IAST) was known as an efficient method for predicting the adsorption selectivity of a multicomponent mixture and estimating the adsorbent's gas separation performance. First, the Langmuir–Freundlich (L–F) model is employed to fit the experimental adsorption data of a single component at a given temperature. The L–F model is described by the following equation [26, 34]:

$$q = q_{sat}\frac{\alpha p^n}{1+\alpha p^n} \quad (1)$$

where q ($cm^3$ $g^{-1}$) is the uptake amount; $q_{sat}$ ($cm^3$ $g^{-1}$) is the saturation uptake capacity on the sites; p (kPa) is the pressure of bulk gas at equilibrium with the adsorbed phase; α ($kPa^{-1}$) is the affinity coefficient of the sites; and n is the coefficient of the L–F model.

Then the $CO_2/N_2$ selectivity was calculated by combining the L–F model with the IAST theory, following the formula below [18, 23, 35, 43]:

$$S_{CO_2/N_2} = \frac{q_{CO_2}/p_{CO_2}}{q_{N_2}/p_{N_2}} \quad (2)$$

where $q_{CO2}$ and $q_{N2}$ are loading amounts of $CO_2$ and $N_2$ in $cm^3$ $g^{-1}$ estimated by IAST, respectively. $p_{CO2}$ and $p_{N2}$ are the partial pressures of $CO_2$ and $N_2$ in kPa, respectively.

### Computational Details

To shed light on the adsorption mechanisms of $CO_2$ and $N_2$ on the boehmite–melamine composite, density functional theory (DFT) calculations were performed using the Gaussian 16 Rev.C.01 package [15] by combining the M06-2X Minnesota functional [46] with the 6–31 + G(d,p) basis set for all the elements, including Al, N, C, O, and H. To improve the accuracy of energy, the highest Pople basis set 6–311 + + G(3df,3pd) was employed. The binding enthalpy and binding free energy of melamine on boehmite and of the gas molecules ($CO_2$, $N_2$) on the composite at 298.15 K and 1 atm conditions were calculated by the difference in the enthalpies or free energies of the product and the ones of the reactants.

## Results and Discussion

### Material Characterizations

Figure 1 shows the XRD pattern of the as-prepared sample from alumina sol by the spray drying method, which disclosed characteristic peaks of the boehmite phase [11, 33] (JCPDS card No. 00–021-1307). This implied that the boehmite sample was successfully fabricated. It is noteworthy that the XRD profile of all modified boehmite samples was in good agreement with that of the pristine sample. No

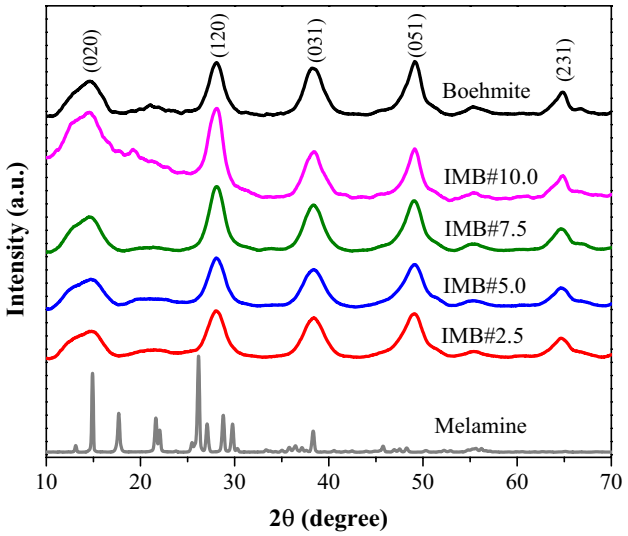


**Fig. 1** XRD patterns of the boehmite and modified melamine–boehmite samples

characteristic peaks of melamine species were detected on these XRD patterns, suggesting that the presence of melamine species had an insignificant effect on the crystal structure of pristine boehmite material. This could be assigned to either a small melamine dose consumed or a uniform dispersion of melamine species in the whole boehmite system.

The SEM results in Fig. 2 illustrate the spherical morphology of the synthesized materials. The diameter of the IMB#x samples is similar to that of the boehmite material, with average particle sizes ranging from 2.20 to 2.48 µm, as shown in Fig. S1. Introducing melamine into the boehmite system does not affect the morphology of the as-prepared materials, but it leads to increased surface roughness. Particularly, observable shreds on the surface of the IMB#10.0 sample, which contains a 10% mole fraction of melamine, illustrate the excessive presence of melamine in the material. Nonetheless, the EDX mapping in Fig. 3 illustrates a good dispersion of N elements across the IMB#x samples, indicating the effective distribution of melamine within the boehmite matrix. Notably, an increasing density of N atoms is observed in SEM–EDX images, following the sequence: IMB#2.5 < IMB#5.0 < IMB#7.5 < IMB#10.0. This suggests a gradual increment in melamine concentration within the IMB#x spheres as the proportion of melamine in the sol mixture increases from 2.5 to 10.0% by mole. This is further substantiated by the determination of the atomic ratio between N and Al, which corresponds to 0.016, 0.025, 0.13, and 0.48 for IMB#2.5, IMB#5.0, IMB#7.5, and IMB#10.0, respectively (Fig. S2).

Figure 4 illustrates a comparison between the FTIR spectra of the as-prepared samples and the pure melamine, which serves as the reference. It could be found that the melamine's FTIR spectrum revealed the characteristic peaks because of strong absorption at wavenumbers of 3470, 3419, 3321, and 3122 $cm^{-1}$ assigned to vibration of N–H bonding belonging to the $–NH_2$ group, while the stretching triazine ring was found at the peaks of 1645, 1522, and 816 $cm^{-1}$ [3, 17, 48]. A characteristic stretch of C–N bonding between the C of the triazine ring and the $–NH_2$ group in the melamine structure is observed at a wavenumber of 1022 $cm^{-1}$ [21]. Similarly, the FTIR profile of the pristine boehmite sample

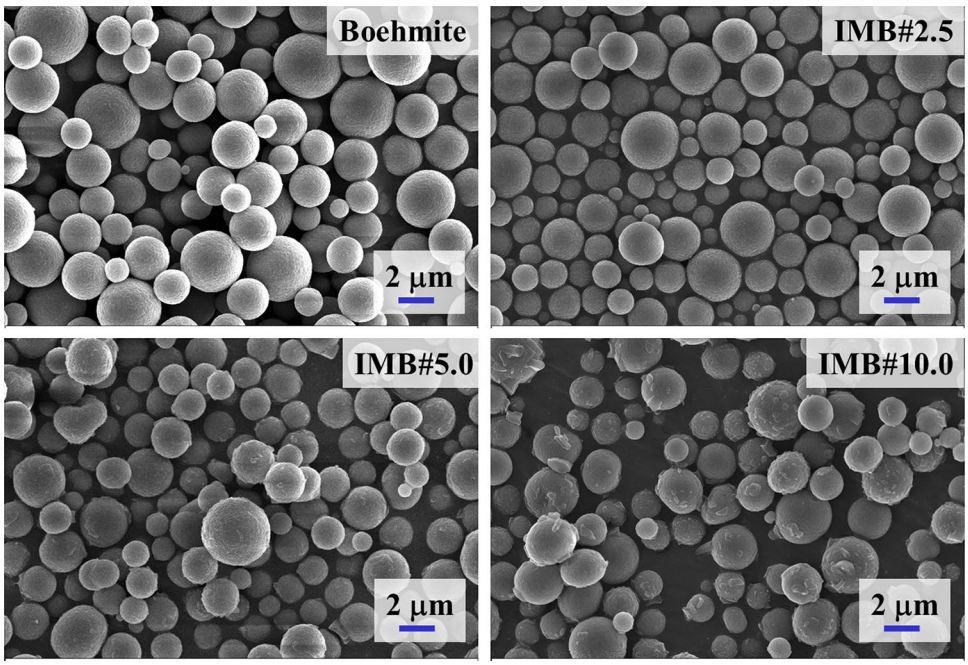


**Fig. 2** SEM images of the as-prepared materials

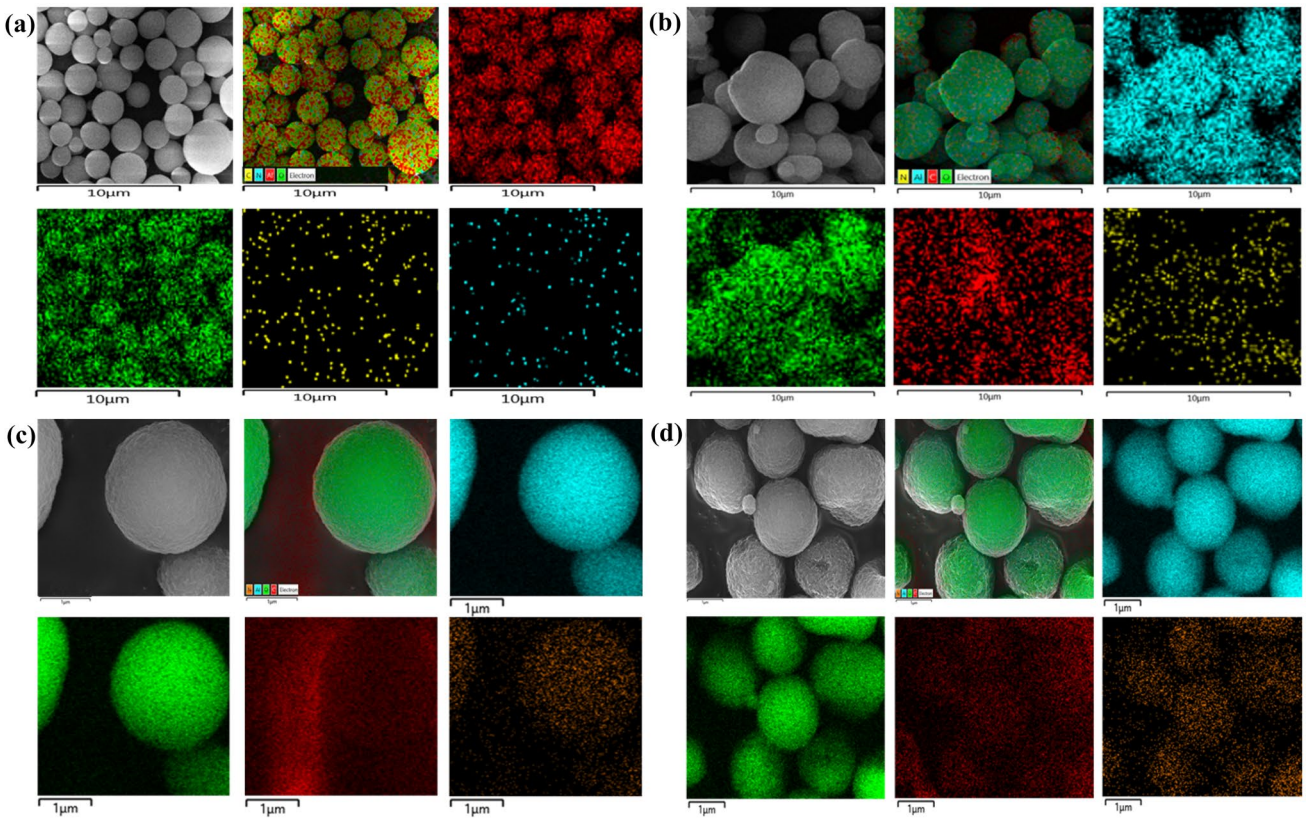


**Fig. 3** EDX mappings of elemental N, Al, C, and O on **a** IMB#2.5, **b** IMB#5.0, **c** IMB#7.5, and **d** IMB#10.0 samples

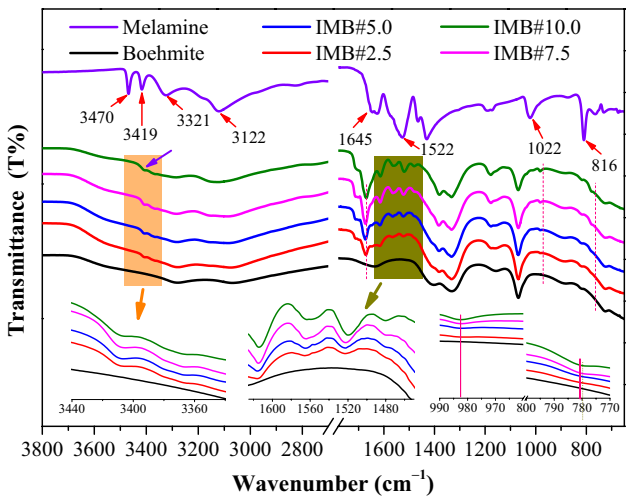


**Fig. 4** FTIR profiles of the as-prepared materials

displayed typical vibrations, which are consistent with previous reports in which the band at 1070 cm$^{-1}$ and region of 3000–3300 cm$^{-1}$ were ascribed to vibrations of the Al−O and O−H bond, respectively [33]. Compared to the original boehmite sample, the FTIR spectra of IMB spherical composites unveiled distinctive peaks readily discerned at the wavenumber of 780 cm$^{-1}$, 980 cm$^{-1}$, and 3400 cm$^{-1}$ for the minor vibrations, as well as in the region of 1500–1600 cm$^{-1}$ and 1675 cm$^{-1}$ for the major bending, as detailed in the inserted figures. These peaks may be ascribed to the interaction of melamine molecules with the boehmite network through H-bonding, resulting in the alteration of melamine's characteristic vibrations. Notably, these peaks were observed with gradual signal intensity increments from IMB#2.5 to IMB#10.0. These findings indicate that melamine has been successfully integrated into the boehmite system.

Figure 5 shows TGA profiles of melamine, pure boehmite, and IMB#5.0 composites, indicating their thermal decomposition behaviors during heat treatment. The pristine boehmite sample shows significant weight loss in two stages, similar to the previous reports. At the beginning stage, a weight loss of around 6% is assigned to eliminate a quantity of moisture physically linked in the materials when heating from ambient temperature to 370 K. Then in the 600–800 K region, a significant weight loss occurs due to a dehydroxylation reaction in which molecular waters are released from boehmite to form aluminum oxide [33, 37]. In the case of the IMB#5.0 sample, overall, the heat degradation process is similar to that of the boehmite sample. Notably, there is

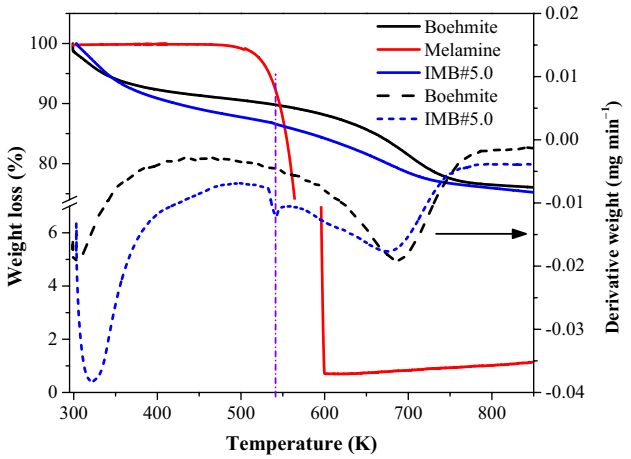


**Fig. 5** TGA curves of the as-prepared materials

a minor weight loss observed at 540 K, as depicted in the derivative weight curves (Fig. 5), which is attributed to the decomposition of melamine.

Figure 6(a) displays the $N_2$ adsorption/desorption isotherms of the pristine and melamine-modified boehmite samples. According to the IUPAC classification, all samples' profiles have type IV characteristic curves with a type H1 hysteresis loop between the adsorption and desorption isotherms, indicating that the materials have a mesoporous structure. Indeed, the pore size distribution, inferred from the desorption curve using the BJH model, demonstrates the mesoporous structure of materials. As shown in Fig. 6(b), all the curves have a main peak located in a region of 3.5–3.9 nm, which falls within the scope of mesoporous material in the range of 2–50 nm. The textural properties of as-prepared samples are disclosed in Table 1, in which the pristine boehmite possesses a BET surface area and total pore volume of 263.6 $m^2\ g^{-1}$ and 0.141 $cm^3\ g^{-1}$, respectively, and a mean pore size of 3.90 nm. As the amount of melamine increases, the specific surface area of the materials decreases from IMB#2.5 to IMB#10.0. This could be due to melamine species penetrating into the pristine boehmite's pore system [40]. Consequently, the centered peak of pore size distribution is gradually shifted from 3.89 to 3.50 nm, corresponding to boehmite and IMB#10.0, respectively, as shown in Fig. 6(b).

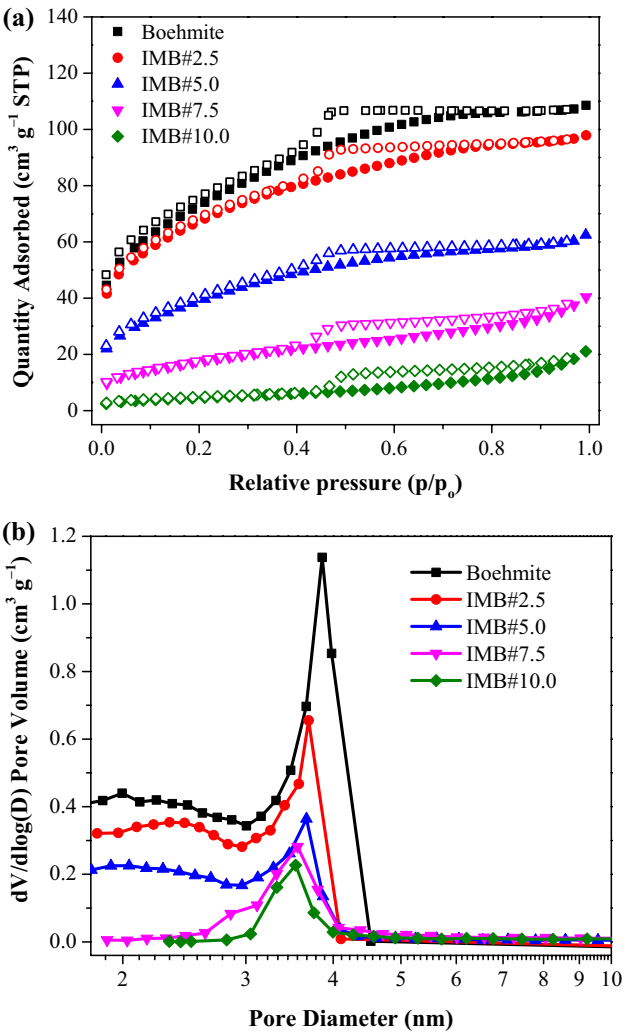


**Fig. 6** **a** $N_2$ adsorption/desorption isotherms at 77 K, and **b** pore size distribution of the as-prepared materials, as calculated from the BJH model

**Table 1** Textural properties of the Boehmite and IMB samples

| Materials | BET surface area ($m^2\ g^{-1}$) | Total pore volume ($cm^3\ g^{-1}$) |
|---|---|---|
| Boehmite | 263.6 | 0.141 |
| IMB#2.5 | 233.8 | 0.116 |
| IMB#5.0 | 143.5 | 0.087 |
| IMB#7.5 | 65.4 | 0.054 |
| IMB#10.0 | 16.6 | 0.033 |

## $CO_2$ and $N_2$ Separation Performance

Figure 7 displays the behavior of the adsorption of $CO_2$ and $N_2$ at 25 °C on the pristine and melamine-modified boehmite samples in the pressure range of 0–100 kPa. It can be seen that all samples show a much higher adsorption capacity of $CO_2$ than that of $N_2$, implying a more vigorous interaction between $CO_2$ molecules and the adsorbents. Indeed, the pristine boehmite reaches an uptake amount of 13 $cm^3\ g^{-1}$ for $CO_2$ and 0.36 $cm^3\ g^{-1}$ for $N_2$ because of the abundant presence of–OH groups, which have a strong affinity for $CO_2$ molecules. Interestingly, after integrating melamine

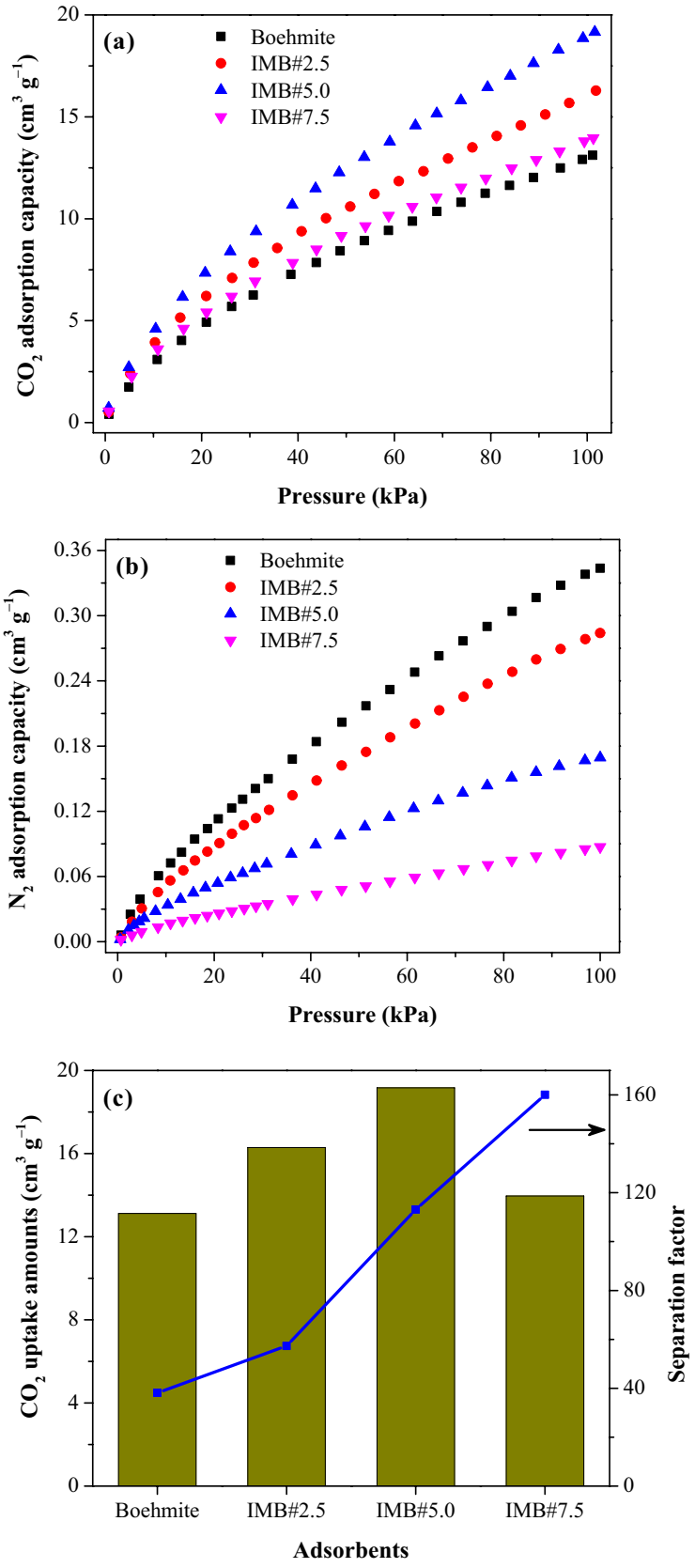


**Fig. 7** $CO_2$ and $N_2$ adsorption properties of the boehmite and modified boehmite samples: **a** $CO_2$ adsorption isotherms, **b** $N_2$ adsorption isotherms, and **c** correlation of $CO_2$ adsorption capacities and $CO_2/N_2$ separation factor

species into the boehmite matrix, $N_2$ adsorption capacities on the composite materials are significantly reduced owing to decreased BET surface area, whereas $CO_2$ uptake amounts are substantially improved. Specifically, the $CO_2$ adsorption capacity increases from 13 to 16 $cm^3\ g^{-1}$ and 20 $cm^3\ g^{-1}$, corresponding to the original boehmite, IMB#2.5, and IMB#5.0 samples, respectively. This result is because of the presence of melamine species incorporated into the composite materials, possessing many functional groups like $-NH_2$ and $-CN$, with strong affinity for $CO_2$ adsorbate. It is worth noting that the $CO_2$ and $N_2$ molecules have very similar kinetic diameters, which are 0.33 nm and 0.36 nm, respectively. Nevertheless, compared to the $N_2$ molecule, the $CO_2$ counterpart has much higher quadrupole moments and polarizability and more free-electron pairs on the oxygen bridge. As a result, the $CO_2$ molecules form preferable bonds to the previously mentioned functional groups through both charge interaction and H-bonding [2, 31]. Nevertheless, a further increase in melamine concentration up to 7.5% led to a reduction in $CO_2$ uptake owing to decreasing porosity. To further elucidate the effect of melamine concentration on the adsorbent's $CO_2$ separation performance, the $CO_2/N_2$ separation factor is used. The separation factor is defined as a ratio of $CO_2$ adsorption capacity over that of $N_2$ at the same adsorptive conditions of temperature and pressure, corresponding to 25 °C and 100 kPa [2, 25]. As shown in Fig. 7(c), the as-made boehmite melamine composites demonstrate a significant improvement in $CO_2/N_2$ separation factor at 25 °C and 100 kPa, corresponding to 38.2, 57.4, 113.1, and 160.0 for boehmite, IMB#2.5, IMB#5.0, and IMB#7.5, respectively.

To estimate effective $CO_2$ separation in a gas mixture, the IAST tool is employed to predict $CO_2/N_2$ selectivity for a mixture of 10% $CO_2$ and 90% $N_2$ at 25 °C in the pressure range of 0–100 kPa. All $CO_2$ and $N_2$ experimental data of boehmite and IMB#x adsorbents are fitted following the L–F model with significant reliability ($R^2 \geq 0.9994$), as shown in Table S1, suggesting that the $CO_2$ and $N_2$ adsorptive behaviors of the boehmite and IMB#x adsorbents are well defined by the L–F model. Figure 8 shows the $CO_2/N_2$ adsorptive selectivity of the boehmite and IMB#x adsorbents inferred from the IAST means, with a gradual improvement in effective separation as bulk pressure increases. Boehmite demonstrates promise as an adsorbent for separating $CO_2$ over $N_2$. Nonetheless, the $CO_2/N_2$ separation performance of IMB#x samples exhibits an even more substantial enhancement through the incorporation of melamine species into the boehmite system. Moreover, a notable improvement in the $CO_2/N_2$ separation performance is observed with an increase in melamine concentration in the boehmite matrix. At 298 K and 1 bar, the boehmite sample reaches an IAST $CO_2/N_2$ selectivity of 268, whereas the IAST $CO_2/N_2$ selectivities are 671, 2030, and 5129 on the IMB#2.5, IMB#5.0, and IMB#7.5 samples, respectively. This is because the structure of IMB#x possesses a large quantity of new adsorption sites ($-NH_2$, $-CN$), originating from integrated melamine molecules on the boehmite matrix, including $-NH_2$ and $-CN$, which have a strong affinity with the $CO_2$ molecules. Considering both the $CO_2$ uptake amount, the $CO_2/N_2$ separation factor, and $CO_2/N_2$ IAST selectivity, the sample with 5.0% melamine (IMB#5.0) was chosen as the best sample because it showed around 46.1% higher $CO_2$ adsorption capacity, a threefold higher $CO_2/N_2$ separation factor, and approximately 7.6 times higher $CO_2/N_2$ selectivity than the pristine boehmite sample.

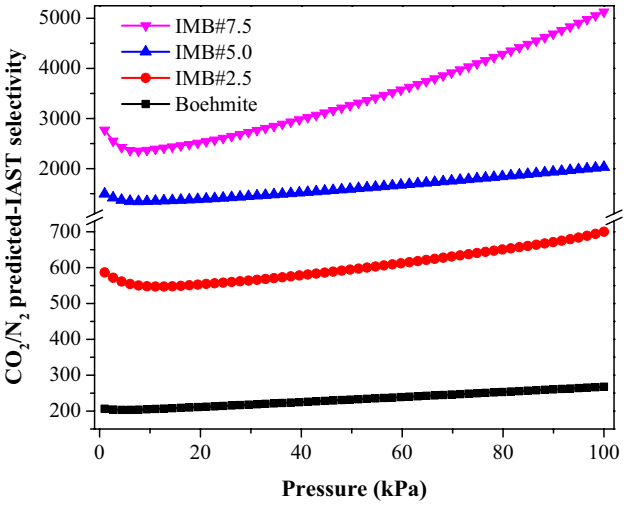


**Fig. 8** IAST-predicted selectivities using $CO_2/N_2$ (0.1/0.9) mixture on boehmite and IMB samples at 298 K

## Isosteric Heat of $CO_2$ Adsorption

Figure. S3 depicts the $CO_2$ adsorptive behavior of the boehmite and IMB#5.0 adsorbents at various temperatures and their isosteric enthalpy of $CO_2$ adsorption. Undoubtedly, the adsorptive interaction between $CO_2$ and the adsorbents is physisorption because of a gradual decrease in $CO_2$ uptake amounts when increasing the adsorption temperature from 15 to 35 °C [27, 42, 47]. Indeed, using the Clausius – Clapeyron equation, the isosteric enthalpy of the $CO_2$ adsorption ($\Delta H$) reaches a range of 25–34 kJ $mol^{-1}$ for IMB#5.0 and 23–25 kJ $mol^{-1}$ for the boehmite sample (Fig. 9), which is within the scope of physical adsorption [24, 26]. Introducing melamine species into the boehmite system contributes to an increase in enthalpy due to new active sites (N functional groups) originating from melamine. Nevertheless, these values are somewhat modest, implying that the refreshment of the IMB#5.0 can be conducted feasibly for recycling. Therefore, to validate this, a series of five sequential cycles of $CO_2$ adsorption was carried out. The findings reveal

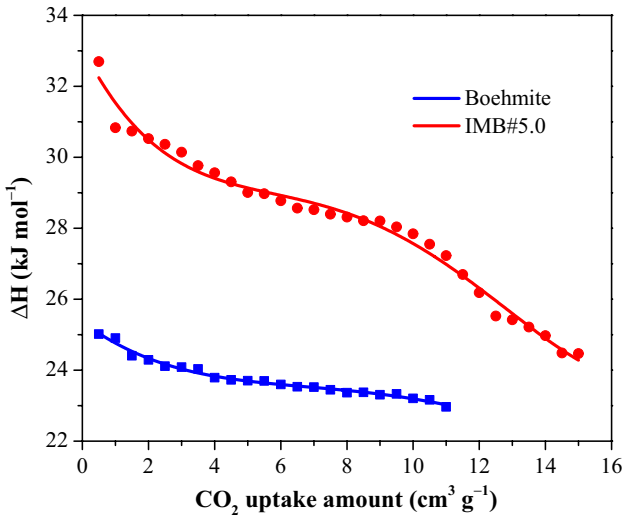


**Fig. 9** Isosteric heat of $CO_2$ adsorption on boehmite and IMB#5.0 samples at 298 K

that the IMB#5.0 sample exhibits substantial $CO_2$ adsorption levels, reaching up to 99% in comparison to the initial sample (Fig. 10(a)). This is further confirmed by the FTIR analysis of the IMB#5.0 sample before and after five-cycle $CO_2$ adsorption. As depicted in Fig. 10(b), there are no significant changes in the vibration of the featured peaks in the range from 1650 to 1500 $cm^{-1}$ and at 1156 $cm^{-1}$, which are attributed to the triazine rings and C–N groups belonging to melamine molecules [7, 32].

## Interaction Configurations of Melamine on Boehmite

To shed light on the structure of the boehmite/melamine composite, we first investigated all possible interaction configurations of melamine molecules on the surface of boehmite using the DFT approach. Cluster models with different sizes, including 4 and 9 AlOOH monomers, were employed to reproduce the boehmite structure (Fig. 11).

As can be seen in Fig. 11(A), only two different cooperative configurations between the melamine and $(AlOOH)_4$ are found in which the melamine molecule interacts either with the Al atom and O one (of Al = O bond) via its N atom of triazine ring and $-NH_2$ group, respectively (mode A1), or with the O atom (of Al = O bond) and −OH group via its $-NH_2$ group and the N atom of triazine ring, respectively (mode A2). The adsorption mode A1 is found to be more stable, with the enthalpy and free energy of binding being − 27.5 and − 11.4 kcal $mol^{-1}$, respectively, compared with the mode A2 (− 10.7 and 2.2 kcal $mol^{-1}$, respectively). Regarding the adsorption of melamine on $(AlOOH)_9$ cluster, seven configurations are observed, with the binding enthalpies and binding free energies ranging

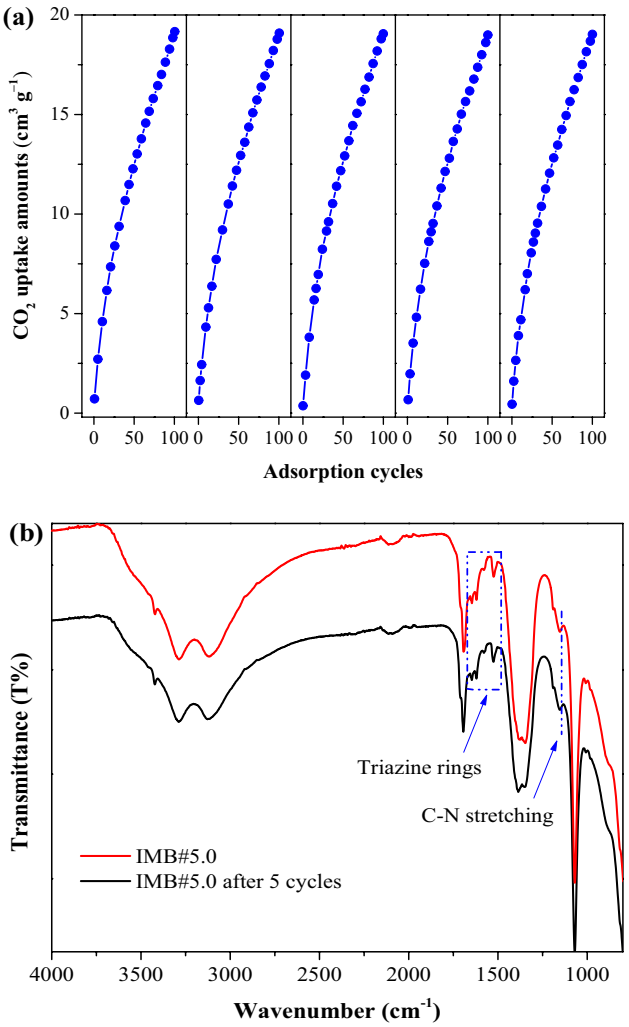


**Fig. 10** **a** Five cycles of $CO_2$ adsorption on IMB#5.0 sample at 298 K and **b** FTIR results of the IMB#5.0 before and after $CO_2$ adsorption performance for five cycles

from − 33.6 to − 10.2 kcal $mol^{-1}$, and from − 15.3 to 2.8 kcal $mol^{-1}$, respectively. It is interesting to note that the most stable interaction configuration of melamine on the $(AlOOH)_9$ cluster (mode B2, Fig. 11(B)) is quite similar to the $(AlOOH)_4$ cluster (mode A1, Fig. 11(A)). Therefore, it is noteworthy that the boehmite/melamine composite may be stabilized by the strong interaction between the N atom of the triazine ring and the Al one, although other configurations may co-exist. Furthermore, the $(AlOOH)_4$ cluster may provide a similar structure to the boehmite/melamine composite when compared with the $(AlOOH)_9$ one. For that reason, we chose the small cluster $(AlOOH)_4$ for further evaluation for the adsorption of gas molecules (i.e., $CO_2$ and $N_2$).

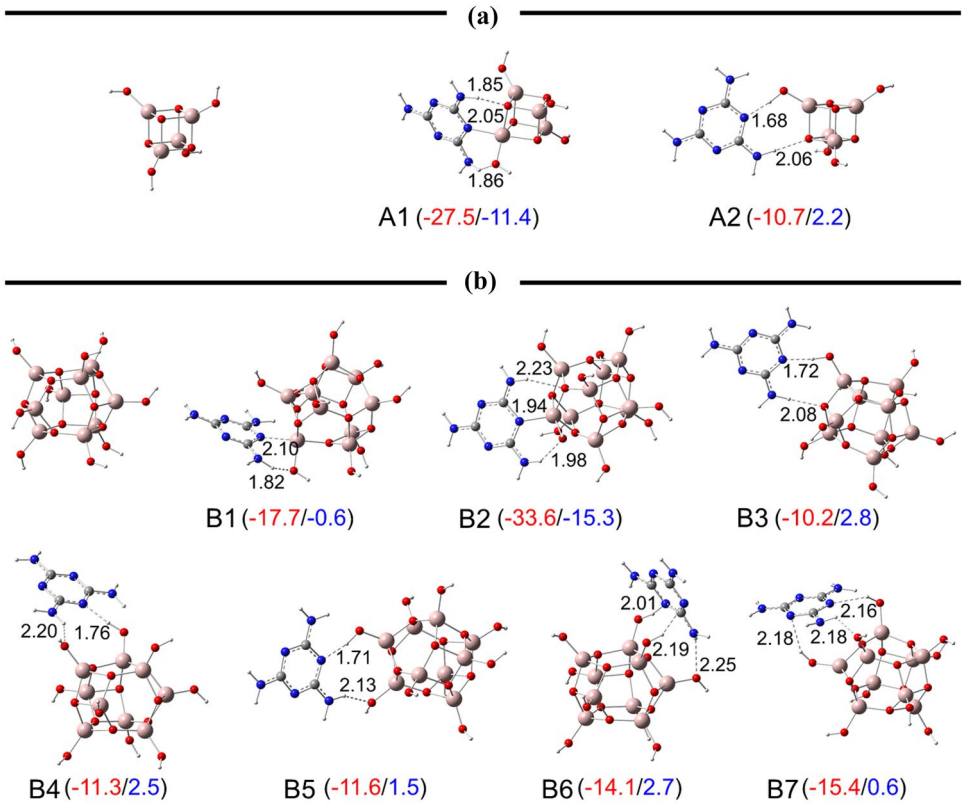


**Fig. 11** Optimized structure of composite of melamine with **A** $(AlOOH)_4$ and **B** $(AlOOH)_9$ calculated in the gas phase at the M06-2X/6–311 + + G(3df,3pd)//M06-2X/6–31 + G(d,p) level of theory. Values in parentheses are binding enthalpies ($H_{bind}$) and binding free energies ($G_{bind}$) (in kcal/mol), respectively

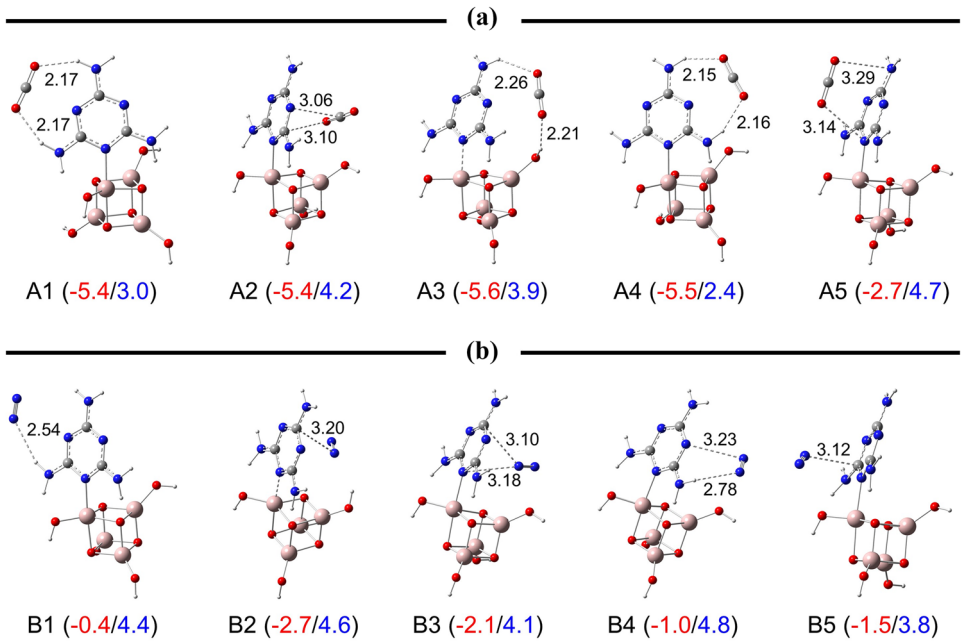


**Fig. 12** Interaction configurations of the composite $(AlOOH)_4$ cluster/melamine with **A** $CO_2$ and **B** $N_2$ calculated in the gas phase at the M06-2X/6–311 + + G(3df,3pd)//M06-2X/6–31 + G(d,p) level of theory. Values in parentheses are binding enthalpies ($H_{bind}$) and binding free energies ($G_{bind}$) (in kcal/mol)

### Adsorption Mechanism of $CO_2$ and $N_2$ on the $(AlOOH)_4$/Melamine Composite

Figure 12 displays the adsorption configurations of $CO_2$ and $N_2$ on the composite $(AlO.OH)_4$/melamine in the gas phase at 298.15 K and 1 atm. As can be seen in Fig. 12A, the $CO_2$ molecule can form either a coplanar complex with melamine via the interaction with both the $–NH_2$ groups (modes A1 and A4) or a parallel complex in which the $CO_2$ molecule is in parallel with the triazine ring (modes A2 and A5). The gas molecule can adsorb on the composite by interacting with the $–NH_2$ and –OH groups (mode A3). The enthalpies and free energies of binding vary from − 5.6 to − 2.7 and from 2.4 to 4.7 kcal $mol^{-1}$, respectively. On the other hand, the $N_2$ molecule interacts with the melamine molecule of the composite via different adsorption configurations, with the binding enthalpies varying from − 2.7 (mode B2) to − 0.4 kcal $mol^{-1}$ (mode B1). The binding free energies vary from 4.1 (mode B3) to 4.8 kcal $mol^{-1}$ (mode B4).

It is noteworthy that the adsorption of $CO_2$ is more favorable than that of $N_2$, with more negative binding enthalpies and free energies. For example, the lowest binding free energy for $CO_2$ adsorption being 2.4 kcal $mol^{-1}$ (mode A4) is 1.4 kcal $mol^{-1}$ lower than the lowest one for $N_2$ adsorption (mode B5, 3.8 kcal $mol^{-1}$). It means that the adsorption of $CO_2$ is more favorable than that of $N_2$, and this will favor the $CO_2$ separation from $N_2$ in their mixture. This observation is in good agreement with the data reported above.

## Conclusion

The successful preparation of spherical, micron-sized particles of both pure and melamine-modified boehmite is achieved using a combination of the sol–gel process and spray drying technology. While increasing the melamine concentration has no impact on crystallinity, it does increase the roughness on the surface of the resulting material, concurrently reducing the BET surface area and total pore volume. As expected, the $CO_2$ uptake amount is still improved over the melamine-modified boehmite samples due to the N-derived functional groups of $–NH_2$ and –CN that play a role as basic sites interacting vigorously with Lewis acid of $CO_2$. The optimized sample of IMB#5.0 showed a $CO_2$ adsorption amount of 19.2 $cm^3$ $g^{-1}$ and a $CO_2/N_2$ separation factor of 113.3 at 25 °C and 1 bar, which are approximately 46.1% and three times higher than the pure boehmite sample, respectively. In addition, the IMB#5.0 sample shows a $CO_2/N_2$ adsorption selectivity based on IAST up to 2030, which is 7.6 times higher than the pristine sample at 25 °C and 1 bar. Simultaneously, the isosteric enthalpy of $CO_2$ adsorption on IMB#5.0 is slightly higher compared to boehmite. The DFT modeling shows that melamine adsorbs on the boehmite structure via the strong interaction between the N atom of the triazine ring and the Al atom of boehmite. And the adsorption of $CO_2$ on the composite is more favorable than that of $N_2$, which has lower binding energies. Considering its excellent $CO_2$ separation performance and affordable large-scale production, IMB#5.0 is promising as a potential adsorbent for $CO_2$ separation on an industrial scale.

**Supplementary Information** The online version contains supplementary material available at https://doi.org/10.1007/s11814-024-00194-2.

**Acknowledgements** This research was supported by Basic Science Research Capacity Enhancement Project through Korea Basic Science Institute (National research Facilities and Equipment Center) grant funded by the Ministry of Education (No. 2019R1A6C1010052) and Basic Science Research Program through the National Research Foundation of Korea(NRF) funded by the Ministry of Education (No. 2020R1A6A1A03048004).

**Data availability** The data is shown in both the manuscript and supporting information files.

## References

1. M. Abdollahifar, M. Hidaryan, P. Jafari, Bol. Soc. Esp. Ceram. V **57**, 66 (2018)
2. H.R. Abid, Z.H. Rada, X. Duan, H. Sun, S. Wang, Energy Fuels **32**, 4502 (2018)
3. T. Arumugham, N.J. Kaleekkal, D. Rana, K.I. Sathiyanarayanan, RSC Adv. **9**, 41462 (2019)
4. C. Avci-Camur, J. Troyano, J. Pérez-Carvajal, A. Legrand, D. Farrusseng, I. Imaz, D. Maspoch, Green Chem. **20**, 873 (2018)
5. K. Bahrami, M.M. Khodaei, M. Roostaei, New J. Chem. **38**, 5515 (2014)
6. F. Banisheykholeslami, M. Hosseini, G.N. Darzi, M.R.S. Kebria, Korean J. Chem. Eng. **40**, 841 (2023)
7. C. Bao, Y. Jiang, L. Zhao, D. Li, P. Xu, J. Sun, New J. Chem. **45**, 13893 (2021)
8. J.M.A. Caiut, J. Dexpert-Ghys, Y. Kihn, M. Vérelst, H. Dexpert, S.J.L. Ribeiro, Y. Messaddeq, Powder Technol. **190**, 95 (2009)
9. S. Carstens, D. Enke, J. Eur. Ceram. Soc. **39**, 2493 (2019)
10. C. Chen, J. Kim, W.-S. Ahn, Korean J. Chem. Eng. **31**, 1919 (2014)
11. K. Cho, J. Kim, H.T. Beum, T. Jung, S.S. Han, J. Hazard. Mater. **344**, 857 (2018)
12. K. Cho, J. Kim, J.-H. Park, T. Jung, H.T. Beum, D.-W. Cho, Y.W. Rhee, S.S. Han, Microporous Mesoporous Mater. **277**, 142 (2019)
13. J. Choi, J. Kim, K.S. Yoo, T.G. Lee, Powder Technol. **181**, 83 (2008)
14. S.P. Dubey, A.D. Dwivedi, M. Sillanpää, H. Lee, Y.-N. Kwon, C. Lee, Chemosphere **169**, 99 (2017)
15. M. J. Frisch, G. W. Trucks, H. B. Schlegel, G. E. Scuseria, M. A. Robb, J. R. Cheeseman, G. Scalmani, V. Barone, G. A. Petersson, H. Nakatsuji, X. Li, M. Caricato, A. V. Marenich, J. Bloino, B. G. Janesko, R. Gomperts, B. Mennucci, H. P. Hratchian, J. V. Ortiz, A. F. Izmaylov, J. L. Sonnenberg, Williams, F. Ding, F. Lipparini, F. Egidi, J. Goings, B. Peng, A. Petrone, T.

Henderson, D. Ranasinghe, V. G. Zakrzewski, J. Gao, N. Rega, G. Zheng, W. Liang, M. Hada, M. Ehara, K. Toyota, R. Fukuda, J. Hasegawa, M. Ishida, T. Nakajima, Y. Honda, O. Kitao, H. Nakai, T. Vreven, K. Throssell, J. A. Montgomery Jr., J. E. Peralta, F. Ogliaro, M. J. Bearpark, J. J. Heyd, E. N. Brothers, K. N. Kudin, V. N. Staroverov, T. A. Keith, R. Kobayashi, J. Normand, K. Raghavachari, A. P. Rendell, J. C. Burant, S. S. Iyengar, J. Tomasi, M. Cossi, J. M. Millam, M. Klene, C. Adamo, R. Cammi, J. W. Ochterski, R. L. Martin, K. Morokuma, O. Farkas, J. B. Foresman and D. J. Fox, "Gaussian 16 rev. C.01", Wallingford, CT (2016)
16. A. Ghorbani-Choghamarani, B. Tahmasbi, F. Arghand, S. Faryadi, RSC Adv. **5**, 92174 (2015)
17. C. Goel, H. Bhunia, P.K. Bajpai, J. Environ. Sci. **32**, 238 (2015)
18. H. Hamyali, F. Nosratinia, A. Rashidi, M. Ardjmand, J. Environ. Chem. Eng. **10**, 107007 (2022)
19. Z. Huang, L. Ying, F. Gong, J. Lu, W. Wang, J. Ding, J. Yan, J. Environ. Chem. Eng. **11**, 109739 (2023)
20. H. Hur, R.J. Reeder, J. Environ. Sci. **65**, 103 (2018)
21. S. Jawaid, F.N. Talpur, H.I. Afridi, S.M. Nizamani, A.A. Khaskheli, S. Naz, Anal. Methods **6**, 5269 (2014)
22. J. Karger-Kocsis, L. Lendvai, J. Appl. Polym. Sci. **135**, 45573 (2018)
23. S. Khalili, M. Jahanshahi, Korean J. Chem. Eng. **38**, 862 (2021)
24. M.A. Khan, S.-W. Kim, R.A.K. Rao, R.A.I. Abou-Shanab, A. Bhatnagar, H. Song, B.-H. Jeon, J. Hazard. Mater. **178**, 963 (2010)
25. A.-R. Kim, T.-U. Yoon, S.-I. Kim, K. Cho, S.-S. Han, Y.-S. Bae, Chem. Eng. J. **348**, 135 (2018)
26. V.N. Le, T.K. Vo, K.S. Yoo, J. Kim, Sep. Purif. Technol. **274**, 119079 (2021)
27. J. Li, A. Bao, J. Chen, Y. Bao, J. Environ. Chem. Eng. **10**, 107021 (2022)
28. P. Li, S. Zheng, P. Qing, Y. Chen, L. Tian, X. Zheng, Y. Zhang, Green Chem. **16**, 4214 (2014)
29. Y. Li, Y. Wang, B. Chen, L. Wang, J. Yang, B. Wang, J. Environ. Chem. Eng. **10**, 108847 (2022)
30. W. Liang, Z. Liu, J. Peng, X. Zhou, X. Wang, Z. Li, Energy Fuels **33**, 493 (2019)
31. G. Lim, K.B. Lee, H.C. Ham, J. Phys. Chem. C **120**, 8087 (2016)
32. Y. Liu, S. Li, Y. Chen, M. Li, Z. Chen, T. Hu, L. Shi, M. Pudukudy, S. Shan, Y. Zhi, Chem. Eng. J. **474**, 145918 (2023)
33. L. Luo, W. Cai, J. Zhou, Y. Li, J. Hazard. Mater. **318**, 452 (2016)
34. L. Mei, T. Jiang, X. Zhou, Y. Li, H. Wang, Z. Li, Chem. Eng. J. **321**, 600 (2017)
35. A.L. Myers, J.M. Prausnitz, AlChE J. **11**, 121 (1965)
36. J.H. Park, M.W. Hong, H.C. Yoon, K.B. Yi, Korean J. Chem. Eng. **39**, 2775 (2022)
37. M. Rajamani, S.M. Maliyekkal, Carbohydr. Polym. **194**, 245 (2018)
38. C. Shang, Z. Wu, W. Duo Wu, X. Dong Chen, Chem. Eng. Sci. **229**, 116080 (2021)
39. K.A. Shuhailath, V. Linsha, S.N. Kumar, K.B. Babitha, A.A. Mohamed, S. Peer Ananthakumar, RSC Adv. **10**, 44773 (2020)
40. K.A. Shuhailath, V. Linsha, S.N. Kumar, K.B. Babitha, A.A. Mohamed, S. Peer Ananthakumar, RSC Adv. **6**, 54357 (2016)
41. R. Snoeckx, A. Bogaerts, Chem. Soc. Rev. **46**, 5805 (2017)
42. T.K. Vo, V.N. Le, V.C. Nguyen, M. Song, D. Kim, K.S. Yoo, B.J. Park, J. Kim, J. Ind. Eng. Chem. **86**, 178 (2020)
43. K.S. Walton, D.S. Sholl, AlChE J. **61**, 2757 (2015)
44. Y. Wei, M. Chang, J. Liu, N. Wang, J.-X. Wang, Nanoscale **14**, 2793 (2022)
45. Z. Yang, Y.S. Lin, Ind. Eng. Chem. Res. **39**, 4944 (2000)
46. Y. Zhao, D.G. Truhlar, Theor. Chem. Acc. **120**, 215 (2008)
47. Z. Zhou, L. Mei, C. Ma, F. Xu, J. Xiao, Q. Xia, Z. Li, Chem. Eng. Sci. **147**, 109 (2016)
48. H. Zhu, S.-A. Xu, RSC Adv. **8**, 17879 (2018)
49. W. Zhu, Y. Wang, F. Yao, X. Wang, H. Zheng, G. Ye, H. Cheng, J. Wu, H. Huang, D. Ye, J. Environ. Sci. **139**, 93 (2024)